arXiv:1406.7829v1 [quant-ph] 30 Jun 2014

Bipartite and tripartite output entanglement in 3-mode optomechanical systems

Ying-Dan Wang,[1,2,3] Stefano Chesi,[1,4] and Aashish A. Clerk[3]

[1] *CEMS, RIKEN, Wako, Saitama 351-0198, Japan*
[2] *Institute of Theoretical Physics, Chinese Academy of Sciences, Beijing 100190, China*
[3] *Department of Physics, McGill University, 3600 rue University, Montreal, QC Canada H3A 2T8*
[4] *Beijing Computational Science Research Center, Beijing 100084, China*

(Dated: July 1, 2014)

We provide analytic insight into the generation of stationary itinerant photon entanglement in a 3-mode optomechanical system. We identify the parameter regime of maximal entanglement, and show that strong entanglement is possible even for weak many-photon optomechanical couplings. We also show that strong tripartite entanglement is generated between the photonic and phononic output fields; unlike the bipartite photon-photon entanglement, this tripartite entanglement diverges as one approaches the boundary of system stability.

PACS numbers: 42.50.Wk, 42.50.Ex, 07.10.Cm

Entanglement is one of the most fascinating and potentially useful aspects of quantum systems. Of particular interest is the generation of entangled itinerant quanta (which can be easily spatially separated), and of true multipartite entanglement (involving irreducible correlations between three or more subsystems). These goals have been the subject of considerable theoretical and experimental work, in a variety of systems spanning quantum optics setups [1, 2], cold atoms [3], superconducting circuits [4–6] and spin qubits [7]. Optomechanical systems [8], where mechanical motion interacts with electromagnetic fields, could be another powerful platform to realize these goals. A key advantage here is the potential to use mechanical motion to entangle disparate subsystems (e.g. microwave and optical photons). A number of schemes to generate entangled photons in optomechanics have been studied theoretically [9–15]. Recent experiments have also demonstrated mechanically-mediated entanglement between two microwave pulses [16].

Here, we analyze theoretically both itinerant and multipartite entanglement in a 3-mode optomechanical system where two cavities are coupled to a single mode of a mechanical resonator (see inset of Fig. 1). This setup has been realized in several recent experiments [17–19]. Previous theory work examined bipartite output entanglement in this system largely numerically [11, 13–15] , focusing on experimentally-challenging strong-coupling regimes [13, 14] or on transient regimes [15]. In contrast, we focus here on generating stationary output entanglement with weak many-photon optomechanical couplings. We provide a complete yet simple *analytic* understanding of the physics. This allows us to illustrate the trade-off between large entanglement and thermal resilience, as well as to identify the parameter regime of maximum entanglement, a regime which corresponds to a simple matching of optomechanical cooperativities. Surprisingly, this condition coincides with the least favorable regime for the generation of intra-cavity entanglement. We also show that entanglement is optimal between time-delayed pairs of wavepackets.

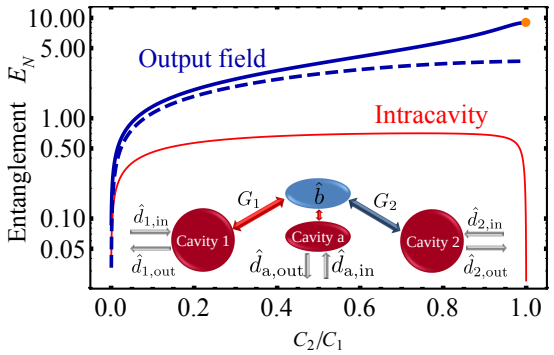

FIG. 1. Inset: Two driven cavities interact with a common mechanical resonator, generating entanglement in the optical outputs. An auxiliary third cavity can be used to cavity cool the mechanics, and to make the mechanical output mode accessible. Main: entanglement of the two cavity output fields on resonance (i.e. $\omega = 0$) (thick blue) and corresponding intracavity entanglement (thin red) as functions of C_2, with $C_1 = 4000$ and $\omega_{\mathrm{m}} \gg \kappa$ (allowing use of the RWA). The orange dot denotes the value of $\ln 2C_1$ as in Eq. (10) with $\kappa_1 \geq \kappa_2$. Results are for zero temperature, except for the blue dashed line (mechanical bath occupancy $N_{\mathrm{m}} = 100$). The output E_N curves only depend on the C_i. For the intracavity curve (thin red), we have also assumed strong coupling, taking $G_1 : \kappa : \gamma = 100 : 10 : 1$.

We also address the generation of tripartite entanglement in such a hybrid 3-mode system, considering correlations between both output photons and phonons. While usually ignored, the mechanical output field could be accessed experimentally, using for example optomechanical crystal geometries with phonon waveguides [20], or by having the mechanical dissipation be dominated by a third auxiliary cavity used for cooling [21]. We find that true hybrid tripartite entanglement is indeed created: the output state corresponds to a "twice-squeezed vacuum", involving the action of two 2-mode squeezing operations involving all three modes. We also quantify this entangle-

ment using the Gaussian Rényi-2 measure [22]. Besides being of fundamental interest, such tripartite entangled states have applications to a variety of quantum information processing tasks such as teleportation, tele-cloning and dense coding [23, 24]. While our emphasis here is on optomechanics, our results also apply to other bosonic 3-mode systems (as could be realized, e.g., with superconducting circuits [25, 26]). The present setup is especially suited to the continous generation of non-local multipartite entanglement, as the phonons and photons from the two cavities are all emitted into spatially separated outputs. Note that Genes et al. [10] also studied tri-partite entanglement in an optomechanical system, though in a setting where the entangled subsystems were not all spatially separated or itinerant.

System and instabilities – The Hamiltonian $\hat{H} = \omega_{\rm m}\hat{b}^\dagger\hat{b} + \sum_{i=1,2}\left[\omega_i\hat{a}_i^\dagger\hat{a}_i + g_i\left(\hat{b}^\dagger+\hat{b}\right)\hat{a}_i^\dagger\hat{a}_i\right] + \hat{H}_{\rm diss}$ governs the system's dynamics, with $\hat{a}_i$ the annihilation operator for cavity i (frequency ω_i, damping rate κ_i), $\hat{b}$ the annihilation operator of the mechanical mode (frequency $\omega_{\rm m}$, damping rate γ), and g_i the optomechanical coupling strengths. $\hat{H}_{\rm diss}$ describes the dissipation of each mode, treated via standard input-output theory [27]. In order to generate steady-state entanglement, cavity 1 (2) is driven at the red (blue) sideband associated with the mechanical resonator: $\omega_{d1} = \omega_1 - \omega_{\rm m}$ and $\omega_{d2} = \omega_2 + \omega_{\rm m}$. By working in an interaction picture with respect to the free Hamiltonian and following the usual linearization procedure [8], we have $\hat{H}^{\rm R} = \hat{H}_{\rm int} + \hat{H}_{\rm CR}(t) + \hat{H}_{\rm diss}$ with

$$\hat{H}_{\rm int} = \left(G_1\hat{b}^\dagger\hat{d}_1 + G_2\hat{b}\hat{d}_2\right) + h.c. = \tilde{G}\left(\hat{b}^\dagger\hat{\beta}_A + h.c.\right), \tag{1}$$

and $\hat{H}_{\rm CR}(t) = \tilde{G}\left(\hat{b}^\dagger\hat{\beta}_A^\dagger e^{2i\omega_{\rm m}t} + h.c.\right)$. Here $\hat{d}_i = \hat{a}_i - \bar{a}_i$ with $\bar{a}_i$ the classical cavity amplitude. $G_i = g_i\bar{a}_i$ is the dressed coupling (we take $g_i, \bar{a}_i > 0$ without loss of generality), $\tilde{G} = \sqrt{G_1^2 - G_2^2}$ and $\hat{\beta}_A = \hat{d}_1\cosh r + \hat{d}_2^\dagger\sinh r$ ($r = \tanh^{-1}(G_2/G_1)$) is a Bogoliubov mode.

We first focus on the resolved-sideband regime $\omega_{\rm m} \gg \kappa_1, \kappa_2$ and make the rotating wave approximation (RWA) by neglecting $\hat{H}_{\rm CR}$ (see [21] for non-RWA corrections).The combined swapping and entangling interactions in $\hat{H}_{\rm int}$ lead to a net entangling interaction between the two cavity modes; as discussed in [28], this interaction has a fundamentally dissipative nature. It is useful to diagonalize $\hat{H}_{\rm int}$ in terms of three normal modes [14, 28]: one "mechanically-dark" Bogoliubov mode $\hat{\beta}_B = \hat{d}_1\sinh r + \hat{d}_2^\dagger\cosh r$ (which is robust to mechanical thermal noise), and two coupled eigenmodes involving both the mechanics and cavities.

Given the blue-detuned laser drive, a first question involves the stability of our linearized system. The Routh-Hurwitz conditions [29] yields two requirements [14, 28] to guarantee stability. The first is that $\gamma_{\rm tot} > 0$, where $\gamma_{\rm tot} = \gamma + 4G_1^2/\kappa_1 - 4G_2^2/\kappa_2$ is the effective damping rate of the mechanical resonator interacting with the two cavities. Focusing on the interesting and relevant regime of strong cooperativities $C_i \equiv 4G_i^2/(\gamma\kappa_i) \gg 1$ and $\kappa_i \gg \gamma$, the two requirements can be combined into:

$$G_1^2/G_2^2 > \max(\kappa_2/\kappa_1, \kappa_1/\kappa_2). \tag{2}$$

Cavity output entanglement – We start by considering the entanglement of light leaving the two cavities. The frequency-resolved output modes $\hat{d}_i^{\rm out}[\omega] \equiv \int d\omega e^{i\omega t}\hat{d}_i^{\rm out}(t)/\sqrt{2\pi}$ are related to the input by $\hat{d}_i^{\rm out}[\omega] = \sum_{j=1}^3 S_{ij}[\omega]\hat{d}_j^{\rm in}[\omega]$ ($j = 3$ denotes the mechanical fields), where the scattering matrix $\mathbf{S}[\omega]$ is obtained straightforwardly from the system Langevin equations (with RWA) and input-output relations, see Eq. (S1) in [21].

For simplicity, we consider output temporal modes in a bandwidth σ centered about the frequency ω described by the following canonical mode operators

$$\hat{D}_i^{\rm out}[\omega, \sigma, \tau_i] = \frac{1}{\sqrt{\sigma}}\int_{\omega-\frac{\sigma}{2}}^{\omega+\frac{\sigma}{2}} d\omega' e^{-i\omega'\tau_i}\hat{d}_i^{\rm out}[\omega']. \tag{3}$$

Here, τ_i sets the absolute time at which the wavepacket of interest is emitted from cavity i; without loss of generality, we set $\tau_2 = 0$. The two-mode entanglement can be quantified using the logarithmic negativity $E_N^{\rm out}[\omega, \sigma, \tau_1]$ [30, 31]. For clarity, we start by discussing the case $\sigma \to 0$; the result is then independent of τ_1 ($\hat{D}_i^{\rm out}[\omega] \equiv \hat{D}_i^{\rm out}[\omega, 0, \tau_i]\, e^{i\omega\tau_i}$, $E_N^{\rm out}[\omega] \equiv E_N^{\rm out}[\omega, 0, \tau_1]$). Later we investigate the role of nonzero σ and the advantage of introducing a finite time delay on cavity 1 output.

We now derive a simple analytic characterization of the output state at $\omega \simeq 0$ (i.e. output light near the cavity resonances) which yields insight into the generation of entanglement. We find that the state has the form of a 2-mode squeezed thermal state:

$$\hat{\rho}_{12} = \hat{S}_{12}(R_{12})\left[\hat{\rho}_1^{\rm th}(\bar{n}_1)\otimes\hat{\rho}_2^{\rm th}(\bar{n}_2)\right]\hat{S}_{12}^\dagger(R_{12}). \tag{4}$$

Here $\hat{S}_{12}(R_{12}) = \exp\left[R_{12}\hat{D}_1^{\rm out}[0]\hat{D}_2^{\rm out}[0] - h.c.\right]$ is the two-mode squeeze operator, with R_{12} the squeezing parameter, and $\hat{\rho}_j^{\rm th}(\bar{n}_j)$ describes a single-mode thermal state with average population $\bar{n}_j$. The output state is thus completely characterized by just 3 parameters: $\bar{n}_1$, $\bar{n}_2$ and R_{12}. In our case, they depend only on cavity cooperativities $C_i = 4G_i^2/(\gamma\kappa_i)$ and bath temperatures. The entanglement of a such a state is found to be [21]:

$$E_N^{\rm out}[0] = -\ln\left(n_R - \sqrt{n_R^2 - (1+2\bar{n}_1)(1+2\bar{n}_2)}\right), \tag{5}$$

with $n_R = (\bar{n}_1 + \bar{n}_2 + 1)\cosh 2R_{12}$.

Assuming first the ideal situation where the cavity and mechanical baths are at zero temperature, we find:

$$\bar{n}_1 = 0, \qquad \bar{n}_2 = 4C_2\frac{\gamma^2}{\gamma_{\rm tot}^2} = \frac{4C_2}{(1+C_1-C_2)^2}, \tag{6}$$

$$\tanh 2R_{12} = \frac{4\sqrt{C_1C_2}(C_2+C_1+1)}{C_1^2+C_2^2+6C_1C_2+2(C_1+C_2)+1}. \tag{7}$$

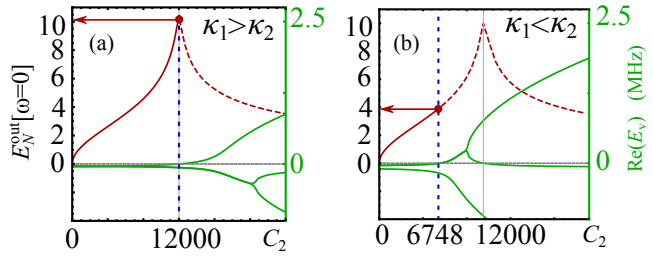

FIG. 2. Output entanglement of the two cavities fields at resonance (i.e. $\omega = 0$) as a function of C_2 for $C_1 = 12000$. In (a), $\kappa_1 > \kappa_2$ ($\kappa_1 = 1.5\kappa_2 = 2\pi \times 0.3$ MHz), in (b) $\kappa_1 < \kappa_2$ ($\kappa_1 = 0.75\kappa_2 = 2\pi \times 0.3$ MHz). Without considering the instability condition, the entanglement would reach a maximum finite value at $C_2 = C_1 + 1$ (gray vertical lines). The green lines show the real part of the three eigenvalues (E_v) of the susceptibility matrix; the system becomes unstable when one of the real parts becomes positive, which is indicated by the blue dashed lines. The red dots indicates the maximum entanglement in each case given the constraints of stability. We used $\gamma = 2\pi \times 10$ KHz. The red dashed line indicates the system has entered the unstable regime.

We stress that the effective thermal occupancies $\bar{n}_j$ are not simply equal to bath temperatures; in particular, $\bar{n}_2 \neq 0$ even when all input noises are vacuum.

Equations (4)-(7) give us a simple way to understand entanglement generation. The ideal situation is when $R_{12} \gg 1$ and $\bar{n}_i \to 0$. From Eq. (7), we see that a large R_{12} generically requires large C_1, C_2. However, Eq. (6) indicates that this limit also yields a large effective temperature for cavity 2 (heuristically, $\hat{H}_{\rm int}$ turns vacuum noise into thermal noise). This heating degrades the purity of the state; however, as $\bar{n}_1$ remains zero, it only slightly degrades the entanglement [28].

From Eqs. (5)-(7), the zero-temperature output entanglement is

$$E_N^{\rm out}[0] = \ln\left(\frac{(1+C_1-C_2)^2}{A+B+2C_2\,(1+2C_1)-4\sqrt{AB}}\right), \quad (8)$$

with $A = C_2\,(C_1+C_2)$, $B = (1+C_1)^2 + C_1C_2$. The approach outlined here can be easily extended to finite temperature (see [21] for discussion). The results at both zero and finite temperature are plotted in Fig. 1.

Optimal output entanglement– Eq. (8) shows that the zero-temperature entanglement is only a function of C_1, C_2, thus weak-coupling does not prevent strong entanglement; for fixed C_1, the expression is optimized when

$$C_2 = C_1 + 1 \equiv C_{2,\rm opt}. \quad (9)$$

Heuristically, this condition corresponds to having a total mechanical damping $\gamma_{\rm tot} = 0$. While $E_N^{\rm out}[0]$ appears to be only a function of the C_i, the ratio κ_1/κ_2 also plays an independent role via the stability condition of Eq. (2). If $\kappa_1 \geq \kappa_2$, $C_{2,\rm opt}$ is also the maximum value of C_2 for which the system is stable. In contrast, if $\kappa_2 \geq \kappa_1$, the system becomes unstable before C_2 reaches $C_{2,\rm opt}$, hence one cannot achieve the optimal amount of entanglement. We thus see that in addition to achieving large C_i it is advantageous to have $\kappa_1 \geq \kappa_2$. Fig. 2 illustrates the behavior of $E_N^{\rm out}[0]$ in these two cases ($C_{2,\rm opt}$ is indicated as a gray vertical line). Note that a similar dependence on κ_1/κ_2 was observed numerically in [14], but in a regime far from optimal entanglement (i.e. for $C_2 \ll C_{2,\rm opt}$).

In the large C_1 limit, the maximum achievable entanglement for the two cases reduces to:

$$E_N^{\rm out}[0]\Big|_{\rm max} \simeq \begin{cases} \ln\left(\frac{2C_1}{1+2N_{\rm m}}\right), & \text{if } \kappa_1 \geq \kappa_2, \\ -\ln\left[\left(\frac{\kappa_2-\kappa_1}{\kappa_2+\kappa_1}\right)^2 + \frac{4\kappa_2^2\kappa_1 N'_{\rm m}}{C_1(\kappa_2+\kappa_1)^3}\right], & \text{if } \kappa_1 < \kappa_2, \end{cases} \quad (10)$$

with $N'_{\rm m} = N_{\rm m}\,(1+\kappa_2/\kappa_1)+1$ and $N_{\rm m}$ the mechanical bath thermal occupancy. In both cases, the output entanglement $E_N^{\rm out}$ is maximal at the boundary of system stability, similar to the behavior of a non-degenerate parametric amplifier (NDPA) [32]. However, unlike a NDPA, $E_N^{\rm out}$ does not diverge at this boundary. Further, while $E_N^{\rm out}$ is maximal at this boundary, the intra-cavity entanglement is extremely sub-optimal at this point. For $\kappa_1 \geq \kappa_2 \gg \gamma$ and $C_2 \simeq C_{2,\rm opt} \gg 1$, one has extremely large entanglement of the output fields while simultaneously having almost zero entanglement of the intracavity fields (see Fig. 1).

Frequency dependence– We now specialize to the case $\kappa_1 = \kappa_2 = \kappa$, $C_j \gg 1$, but vary the output mode center frequency ω. We consider two generic regimes. The first is that of equal couplings $G_1 = G_2 = G$ (i.e., $C_1 = C_2$) which, as discussed, is essentially optimal for maximizing $E_N^{\rm out}[0]$ (it is also an ideal point to generate quantum-limited amplification [33]). In this regime, the effective coupling $\tilde{G}$ in Eq. (1) vanishes, meaning that the three normal modes of $\hat{H}_{\rm int}$ are degenerate. Consequently, the $\sigma = 0$ entanglement spectrum $E_N^{\rm out}[\omega]$ has a single peak at $\omega = 0$ (see thick curves in Fig. 3) of width $\sim \gamma C^{3/4}$ in the weak-coupling case and $\sim \sqrt{G}\left(2\kappa^5\gamma\right)^{1/12}$ in the strong-coupling case. $E_N^{\rm out}[0,\sigma,\tau_1]$ decays on a similar scale as a function of mode bandwidth σ, if one appropriately optimizes the time delay $\tau_1 \sim \kappa/(4G^2)$; without including this delay, the decay with σ is much more pronounced (see Fig. 3b). We stress that achieving large optimal E_N in this regime only requires strong cooperativities, and not the more stringent strong coupling condition $G_j > \kappa_j$ (c.f. Eq. (10)).

Keeping $\kappa_1 = \kappa_2$ and $C_j \gg 1$, another generic regime is where G_2/G_1 is sufficiently smaller than 1 such that the effective coupling $\tilde{G}$ is larger than κ, γ; this necessarily requires $G_1 > \kappa$. In this regime, the three normal modes of $\hat{H}_{\rm int}$ are spectrally resolved and $E_N^{\rm out}[\omega]$ has correspondingly three peaks [14]. The entanglement at $\omega = 0$ is necessarily much smaller than the optimal value

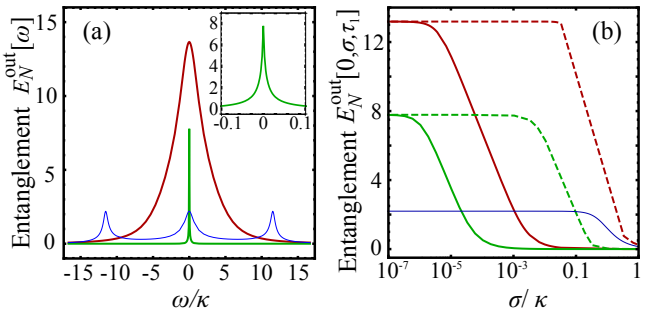

FIG. 3. (a) Output entanglement in the limit of small mode bandwidth ($\sigma \to 0$) as a function of mode center frequency ω, for 3 cases: strong equal-coupling (red thick upper line, $G_1 = G_2 = 13.3\kappa$), weak equal-coupling (green thick lower line, $G_1 = G_2 = 0.1\kappa$) and resolved normal-modes (blue thin line, $G_1/\kappa = 13.3$ and $G_2/\kappa = 6.7$. For the the blue and red curves, $\gamma/\kappa = 1.67 \times 10^{-3}$ while for the green curve $\gamma/\kappa = 3.3{\times}10^{-5}$. The inset shows a zoom-in of the green curve (weak coupling case). (b) Effects of non-zero mode bandwidth σ on the output entanglement of modes with center frequency $\omega = 0$; colors correspond to same parameters as in (a). The solid lines are for zero time-delay between the two cavity output modes ($\tau_1 = 0$, c.f. Eq. (3)) while the dashed lines are the result including an optimal time delay $\tau_1 = \kappa/(4G^2)$.

in Eq. (10). One finds that $C_1 \gg 1$ is not by itself enough to ensure large E_N in this regime; one also needs to be deep in the strong coupling regime, $G_1 \gg \kappa$. As discussed in [14], this "resolved-modes" regime does however offer enhanced protection against mechanical thermal noise, as the central peak is due to the mechanically-dark normal mode β_B.

Finally we note that, in contrast to the intracavity case [28], output entanglement generation is extremely sensitive to any internal cavity loss κ' and $E_N[0]$ is bounded by $\ln(\kappa_{\rm tot}/\kappa')$ [21], where $\kappa_{\rm tot} = \kappa + \kappa'$.

Hybrid 3-mode entangled state – As discussed in the introduction, experimental setups using optomechanical crystals [20, 34] could access the mechanical output field via engineered phonon waveguides. Alternatively, the mechanical output can be accessed by having mechanical dissipation dominated by an auxiliary cooling cavity (Fig. 1); see [21] for details. Motivated by these possibilities, we now consider the multi-partite entanglement properties of all three output fields in our system. Note that previous work studied the non-stationary tripartite entanglement of intracavity fields generated by the *closed-system* Hamiltonian $\hat{H}_{\rm int}$ in Eq. (1) [35]; in contrast, our focus here is on the steady-state output entanglement in our *dissipative* 3-mode system.

We focus on zero frequency and zero bandwidth, and consider the ideal case where all dissipative baths are at zero temperature. In this case, the 3-mode output state is pure, and can be written as a twice-squeezed vacuum [21]:

$$|\Psi\rangle = \hat{S}_{12}\left(R_{12}\right)\hat{S}_{2\rm m}\left(R_{2\rm m}\right)|000\rangle\,, \qquad (11)$$

where $\hat{S}_{2\rm m}\left(R_{2\rm m}\right) \equiv \exp\left[iR_{2\rm m}\hat{D}_{\rm m}^{\rm out}\left[0\right]\hat{D}_{2}^{\rm out}[0] - h.c.\right]$ is the 2-mode squeeze operator entangling the output of the mechanics at $\omega = 0$ (denoted by $\hat{D}_{\rm m}^{\rm out}\left[0\right]$, which is defined in a similar way as the cavity output) with that of cavity 2. The squeezing parameter is $R_{2\rm m} = \sinh^{-1}\bar{n}_2$, where $\bar{n}_2$ is given in Eq. (6) and diverges at the instability point. Equation (11) demonstrates that the effective temperature $\bar{n}_2$ which degraded the cavity-cavity entanglement in Eq. (5) is a direct consequence of entanglement between cavity 2 and the mechanics. It also demonstrates the asymmetry between the three modes (i.e., there is no direct squeezing between the mechanical and cavity 1 outputs.)

More strikingly, Eq. (11) shows that we have genuine tripartite entanglement (GTE): none of the parties can be separated from any other in a mixture of product states, implying a fully inseparable state [36, 37]. To see this, note that the total state is pure, and if one traces over one subsystem, the remaining two are in a mixed state. GTE is also evident by writing the state in the Fock-state basis $|n_1, n_2, n_{\rm m}\rangle$,

$$|\Psi\rangle = \sum_{pq} \frac{\sqrt{C_{p+q}^{p}}\,\langle N_{\rm m}\rangle^{\frac{q}{2}}\,\langle N_1\rangle^{\frac{p}{2}}}{\left(1+\langle N_2\rangle\right)^{(p+q+1)/2}}\,|p, p+q, q\rangle\,, \qquad (12)$$

where C_{p+q}^{p} are binomial coefficients and $\langle N_i\rangle = \left\langle \left(\hat{D}_i^{\rm out}[0]\right)^{\dagger}\hat{D}_i^{\rm out}[0]\right\rangle$ $(i = 1, 2, {\rm m})$ is the average photon/phonon number of each mode (see [21] for their values). $|\Psi\rangle$ only involves Fock states $|n_1, n_2, n_{\rm m}\rangle$ where $n_2 = n_1 + n_{\rm m}$; there is thus a perfect correlation between the three systems that is only evident by looking at all three modes. If any two modes are traced out, the remaining third mode is in an impure thermal state. Notice that, in the absence of dissipation, a similar correlated state of intra-cavity quanta can be generated by the Hamiltonian in Eq. (1) [21, 35].

GTE can also be quantified using the Gaussian Rényi-2 measure recently introduced in [22]. We find that it is indeed non-zero, and diverges as one increases C_2 to the instability point $C_1 + 1$ (due to the divergence of $\bar{n}_2$ and $R_{2\rm m}$) [21]. These calculations also reveal the absence of any direct entanglement between the mechanical and cavity 1 outputs.

Conclusion – We have studied the bipartite and tripartite entanglement of the output fields in a 3-mode optomechanical system. For bipartite photonic entanglement, an explicit analytical expression enables us to obtain an impedance matching condition which yields maximal entanglement. We also have shown that the three output fields are in a genuine tripartite entangled state, with entanglement diverging near the boundary of system stability.

We thank M. Woolley for useful discussions. This work was supported by the DARPA ORCHID program under

a grant from the AFOSR. SC and YDW acknowledge support from Chinese Youth 1000 Talents Program.

Note added.- During the preparation of this work, we came to learn of a related work by Deng, Habraken, and Marquardt looking at different aspects of output light entanglement in an optomechanical system.

[1] T. Aoki, N. Takei, H. Yonezawa, K. Wakui, T. Hiraoka, A. Furusawa, and P. van Loock, Phys. Rev. Lett. **91**, 080404 (2003).

[2] J.-W. Pan, Z.-B. Chen, C.-Y. Lu, H. Weinfurter, A. Zeilinger, and M. Żukowski, Rev. Mod. Phys. **84**, 777 (2012).

[3] J. Raimond, M. Brune, and S. Haroche, Rev. Mod. Phys. **73**, 565 (2001).

[4] M. Neeley, R. C. Bialczak, M. Lenander, E. Lucero, M. Mariantoni, D. Sank, H. Wang, M. Weides, J. Wenner, Y. Yin, T. Yamamoto, A. N. Cleland, and J. M. Martinis, Nature **467**, 570 (2010).

[5] L. DiCarlo, M. Reed, L. Sun, B. L. Johnson, J. M. Chow, J. M. Gambetta, L. Frunzio, S. M. Girvin, M. H. Devoret, and R. J. Schoelkopf, Nature **467**, 574 (2010).

[6] E. Flurin, N. Roch, F. Mallet, M. H. Devoret, and B. Huard, Phys. Rev. Lett. **109**, 183901 (2012).

[7] H. Bernien, B. Hensen, W. Pfaff, G. Koolstra, M. S. Blok, L. Robledo, T. H. Taminiau, M. Markham, D. J. Twitchen, L. Childress, and R. Hanson, Nature **497**, 86 (2013).

[8] M. Aspelmeyer, T. J. Kippenberg, and F. Marquardt, arXiv:1303.0733 (2013).

[9] M. Paternostro, D. Vitali, S. Gigan, M. Kim, C. Brukner, J. Eisert, and M. Aspelmeyer, Phys. Rev. Lett. **99**, 250401 (2007).

[10] C. Genes, A. Mari, P. Tombesi, and D. Vitali, Phys. Rev. A **78**, 032316 (2008).

[11] C. Wipf, T. Corbitt, Y. Chen, and N. Mavalvala, New J. Phys. **10** (2008).

[12] S. G. Hofer, W. Wieczorek, M. Aspelmeyer, and K. Hammerer, Phys. Rev. A **84**, 052327 (2011).

[13] S. Barzanjeh, M. Abdi, G. Milburn, P. Tombesi, and D. Vitali, Phys. Rev. Lett. **109**, 130503 (2012).

[14] L. Tian, Phys. Rev. Lett. **110**, 233602 (2013).

[15] M. C. Kuzyk, S. J. van Enk, and H. Wang, Phys. Rev. A **88**, 062341 (2013).

[16] T. A. Palomaki, J. D. Teufel, R. W. Simmonds, and K. W. Lehnert, Science **342**, 710 (2013).

[17] C. Dong, V. Fiore, M. C. Kuzyk, and H. Wang, Science **338**, 1609 (2012).

[18] J. T. Hill, A. H. Safavi-Naeini, J. Chan, and O. Painter, Nat. Commun. **3**, 1196 (2012).

[19] R. Andrews, R. W. Peterson, T. P. Purdy, K. Cicak, R. W. Simmonds, C. A. Regal, and K. W. Lehnert, Nat. Phys. **10**, 321 (2014).

[20] A. H. Safavi-Naeini and O. Painter, New J. Phys. **13**, 013017 (2011).

[21] See the EPAPS for discussions on scattering matrix, finite temperature, finite bandwidth, internal loss, non-RWA correction, auxiliary cavity for phonon output, and the detailed characterization of tripartite entanglement.

[22] G. Adesso, D. Girolami, and A. Serafini, Phys. Rev. Lett. **109**, 190502 (2012).

[23] S. Braunstein and P. van Loock, Rev. Mod. Phys. **77**, 513 (2005).

[24] S. Koike, H. Takahashi, H. Yonezawa, N. Takei, S. L. Braunstein, T. Aoki, and A. Furusawa, Phys. Rev. Lett. **96** (2006).

[25] N. Bergeal, R. Vijay, V. E. Manucharyan, I. Siddiqi, R. J. Schoelkopf, and M. Devoret, Nature Phys. **296** (2010).

[26] Baust, A. et. al., arXiv:1405.1969.

[27] C. Gardiner and P. Zoller, *Quantum Noise*, 3rd ed. (Springer, New York, 2004).

[28] Y.-D. Wang and A. A. Clerk, Phys. Rev. Lett. **110**, 253601 (2013).

[29] E. X. DeJesus and C. Kaufman, Phys. Rev. A **5288**, 35 (1987).

[30] G. Vidal and R. F. Werner, Phys. Rev. A **65**, 032314 (2002).

[31] M. B. Plenio, Phys. Rev. Lett. **95**, 090503 (2005).

[32] D. F. Walls and G. J. Milburn, *Quantum optics* (Springer, Berlin, 1994).

[33] A. Metelmann and A. A. Clerk, Phys. Rev. Lett. **112**, 133904 (2014).

[34] M. Eichenfield, J. Chan, R. M. Camacho, K. J. Vahala, and O. Painter, Nature **461**, 78 (2009).

[35] A. Ferraro, M. G. A. Paris, M. Bondani, A. Allevi, E. Puddu, and A. Andreoni, J. Opt. Soc. Am. B **21**, 1241 (2004).

[36] G. Giedke, B. Kraus, M. Lewenstein, and J. I. Cirac, Phys. Rev. A **64**, 052303 (2001).

[37] P. van Loock and S. L. Braunstein, Phys. Rev. Lett. **84**, 3482 (2000).

SUPPLEMENTAL INFORMATION

SCATTERING MATRIX

The scattering matrix $\mathbf{S}[\omega]$ is obtained via the system Langevin equations (with RWA) and input-output relations. In our interaction picture:

$$\mathbf{S}[\omega]=\mathbf{1}+\frac{1}{C_1\chi_1\chi_{\rm m}-C_2\chi_2\chi_{\rm m}+1}\begin{pmatrix}\chi_1\left(\frac{C_2}{4}\chi_2\chi_{\rm m}-1\right) & \frac{\sqrt{C_1C_2}}{4}\chi_1\chi_2\chi_{\rm m} & \frac{iC_1}{2}\chi_1\chi_{\rm m}\\ -\frac{\sqrt{C_1C_2}}{4}\chi_1\chi_2\chi_{\rm m} & -\chi_2\left(\frac{C_1}{4}\chi_1\chi_{\rm m}+1\right) & -\frac{iC_2}{2}\chi_2\chi_{\rm m}\\ \frac{iC_1}{2}\chi_1\chi_{\rm m} & \frac{iC_2}{2}\chi_2\chi_{\rm m} & -\chi_{\rm m}\end{pmatrix}, \tag{S1}$$

with $\chi_i=2\kappa_i/(\kappa_i-2i\omega)$ ($i\in\{1,2,m\}$, $\kappa_{\rm m}\equiv\gamma$). Notice that at $\omega=0$, $\chi_i=2$, the matrix only depends on the cooperativities.

BIPARTITE ENTANGLEMENT AT FINITE TEMPERATURE

Mapping to a two-mode squeezed thermal state

Using the standard approach (i.e. plugging the system covariance matrix into the definition of logarithmic negativity), the entanglement of the 3-mode system can be easily computed numerically. However, we find that mapping the output state to a 2-mode squeezed thermal state can yield a simple analytical expression which reveals a number of intresting properties of the output entanglement.

It can be seen from the Langevin equation of the system that $\left\langle \hat{D}_i^{\rm out}[\omega]\right\rangle$ are all zero and only 3 correlators of the output cavity modes are nonzero: $\left\langle \left(\hat{D}_1^{\rm out}[\omega]\right)^\dagger \hat{D}_1^{\rm out}[\omega]\right\rangle$, $\left\langle \left(\hat{D}_2^{\rm out}[\omega]\right)^\dagger \hat{D}_2^{\rm out}[\omega]\right\rangle$ and $\left\langle \hat{D}_1^{\rm out}[\omega]\,\hat{D}_2^{\rm out}[\omega]\right\rangle$. A two-mode squeezed thermal state has the same covariance matrix. Since two Gaussian states with the same covariance matrix represent the same state, this output cavity state can be mapped to a two-mode squeezed thermal state whose non-zero correlation function are simply

$$\begin{aligned}\left\langle \left(\hat{D}_i^{\rm out}[\omega]\right)^\dagger \hat{D}_i^{\rm out}[\omega]\right\rangle &= \bar{n}_i+(\bar{n}_1+\bar{n}_2+1)\sinh^2|R_{12}[\omega]|\,,\\ \left\langle \hat{D}_1^{\rm out}[\omega]\,\hat{D}_2^{\rm out}[\omega]\right\rangle &= -e^{i\theta[\omega]}(\bar{n}_1+\bar{n}_2+1)\sinh|R_{12}[\omega]|\cosh|R_{12}[\omega]|\,,\end{aligned} \tag{S2}$$

where $\bar{n}_i\equiv\bar{n}_i[\omega]$, $R_{12}[\omega]$ is complex in general and $\theta[\omega]\equiv\arg(R_{12}[\omega])$. Plugging in the correlators with $\sigma=0$ and $\omega=0$, we find R_{12} is real and the output state can be characterized with the 3 parameters

$$\begin{aligned}\bar{n}_1&=\frac{1}{2}\left(\frac{4N_{\rm m}}{C_1-C_2+1}-\frac{4(C_2+N_{\rm m})}{(C_1-C_2+1)^2}+\frac{\sqrt{E^2-D^2}}{(C_1-C_2+1)^2}-1\right),\\ \bar{n}_2&=\frac{1}{2}\left(\frac{-4N_{\rm m}}{C_1-C_2+1}+\frac{4(C_2+N_{\rm m})}{(C_1-C_2+1)^2}+\frac{\sqrt{E^2-D^2}}{(C_1-C_2+1)^2}-1\right),\\ \tanh 2R_{12}&=D/E,\end{aligned} \tag{S3}$$

with

$$D=4\sqrt{C_1C_2}(C_1+C_2+1+2N_{\rm m}), \tag{S4}$$

$$E=(C_1+C_2)^2+2(C_1+C_2)(1+2N_{\rm m})+1+4C_1C_2. \tag{S5}$$

Notice that such a mapping is unique, i.e., there isn't an alternate choice of $\bar{n}_1$, $\bar{n}_2$ and R_{12} that yields the same covariance matrix. At zero temperature, the parameters are reduced to Eqs. (6)-(7) of the main text.

Plugging Eq. (S3) into Eq. (5) of the main text, one can obtain the general result of entanglement at finite temperature. Up to linear order in $N_{\rm m}$, it reads

$$E_N^{\rm out}[0]\approx E_N^{\rm out,(0)}[0]+\left(C_1+C_2-\sqrt{\frac{(1+2C_1)^2C_2(C_1+C_2)}{1+C_1^2+C_1(2+C_2)}}\right)\frac{4N_{\rm m}}{(C_1-C_2+1)^2}+O(N_{\rm m}^2), \tag{S6}$$

where $E_N^{\rm out,(0)}[0]$ is the entanglement at zero temperature as shown in Eq. (8) of the main text.

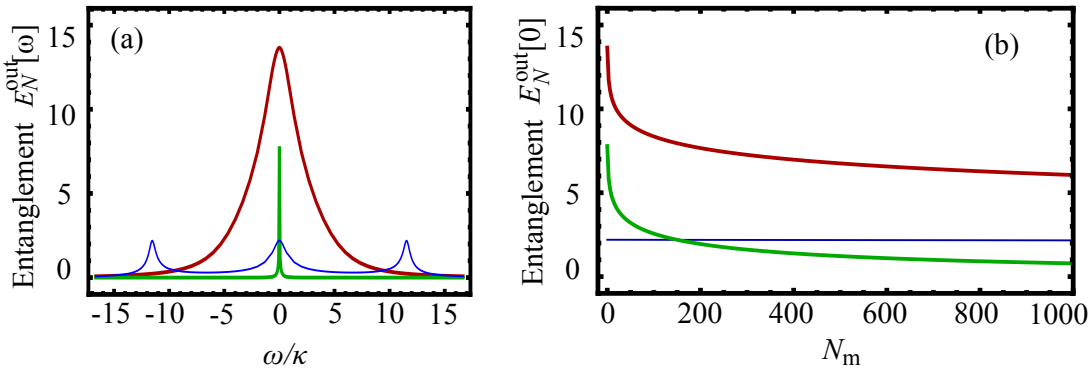

FIG. 4. Output entanglement for 3 cases: strong equal couplings (thick red (upper) lines, $G/\kappa = 13.3$), weak equal couplings (thick green (lower) lines, $G/\kappa = 0.1$) and resolved normal modes (blue thin lines, $G_1/\kappa = 13.3$ and $G_2/\kappa = 6.7$). Panel (a) is a re-plot of Fig. 3(a) in the main text, showing the spectrum of output entanglement with $N_{\rm m} = 0$. Panel (b) shows the output entanglement at $\omega = 0$ *vs.* mechanical temperature N_m. For the green curves, $\gamma/\kappa = 3.3 \times 10^{-5}$; and for the rest, $\gamma/\kappa = 1.67 \times 10^{-3}$.

Entanglement spectrum

As discussed in the main text, the bipartite entanglement of the cavity output modes can be quantified using the logarithmic negativity and for now we discuss the spectrum of entanglement without considering finite bandwidth, i.e. $E_N^{\rm out}[\omega] \equiv E_N^{\rm out}[\omega, 0, \tau_1]$. When $G_1 = G_2$ and $\kappa_1 = \kappa_2$, there is only one peak centered at $\omega = 0$ in the spectrum of the output entanglement as shown by the red and green thick curves in Fig. 4 (a) (a re-plot of Fig. 3(a) of the main text). The peak value at $\omega = 0$ is independent of strong-coupling condition

$$E_N^{\rm out}[0] \approx \ln\left(\frac{2C}{1+2N_{\rm m}}\right) + \mathcal{O}\left(C^{-1}\right), \tag{S7}$$

In the regime of sufficiently strong coupling, we find a simple expression for the half width at half maximum (HFHM) of this peak: $\Delta\omega \approx \sqrt{G}\left(2\kappa^5\gamma\right)^{1/12}$ under the condition that $(G/\kappa)^6 > \kappa/\gamma \gg 1$ and $C \gg 1$. We stress that a robust peak in $E_N^{\rm out}[\omega]$ remains in the weak-coupling case $G < \kappa$ as long as $C \gg 1$; the HWHM is $\Delta\omega \approx \gamma(2C)^{3/4}$.

The entanglement at $\omega = 0$ in the equal-coupling regime shows a prominent decrease with temperature due to the mechanical thermal noise. At low temperature, the equal-coupilngs ($G_1 = G_2$) regime yields a decent entanglement even for weak coupling ($\kappa > G$) as shown by the green curve in Fig. 4 (b).

We turn now to the regime where $\tilde{G} = \sqrt{G_1^2 - G_2^2} > \kappa$, where the three normal modes of the interaction Hamiltonian in Eq. (1) of the main text are spectrally resolved. In this regime (as discussed in [1]), $E_N^{\rm out}[\omega]$ has three peaks, with each peak corresponding to a normal mode. The "dark mode" β_B corresponds to the peak at $\omega = 0$, while the peaks at $\pm\tilde{G}$ are the coupled "hybrid" modes (see blue thin curve in Fig. 4 (a)); all have width $\sim \kappa$. In the simple case $\kappa_1 = \kappa_2$, resolving the normal modes requires $G_1 > \kappa \cosh r \gg \kappa$, i.e., deep in the strong coupling regime for a large r. For typical parameters, the maximum entanglement in the resolved-peaks regime is far less that the optimal value that would be achieved if C_2 were increased to C_1 (see Fig. 4 (b)). On the other hand, the output entanglement at the central peak can be written as (assuming $N_{\rm m}e^{2r} \ll \tilde{C}$)

$$E_N^{\rm out}[0] \approx 4r - 2e^{2r}\left(2N_{\rm m}+1\right)/\tilde{C}, \tag{S8}$$

with the effective cooperativity $\tilde{C} = 4\tilde{G}^2/\gamma\kappa$. This shows that, as the central peak corresponds to the dark mode, the mechanical noise is suppressed by the effective cooperativity and the entanglement is robust to thermal fluctuation as shown in Fig. 4 (b). The entanglement at the side peaks is still sensitive to thermal noise and in the large r limit:

$$E_N^{\rm out}\left[\omega = \pm\tilde{G}\right] \approx 2r - \ln\left(\frac{4\gamma}{\kappa}\left(N_{\rm m} + \frac{1}{2}\right)\right), \tag{S9}$$

valid if $\gamma N_{\rm m}/\kappa \ll 1$.

INFLUENCE OF CAVITY INTERNAL LOSSES ON THE BIPARTITE ENTANGLEMENT

In contrast to the generation of intracavity entanglement [2], the output entanglement is sensitive to the internal losses of the cavities. With internal loss, the total cavity damping rate becomes $\kappa_{tot} = \kappa + \kappa'$, where κ' describes internal loss, and κ is associated with the coupling to the output field. We discuss the influence of internal loss in the following two limiting cases.

1) Equal coupling case. With finite internal loss $\kappa_1' = \kappa_2' = \kappa'$ and also assuming $G \gg \gamma$, κ, κ', the entanglement reads

$$E_N^{\text{out}}[0] \approx -\ln\left(\frac{\kappa'}{\kappa'+\kappa} + \frac{1}{2C}\right), \tag{S10}$$

which recovers the two limits: $E_N^{\text{out}}[0] \approx \ln 2C$ at large κ (still, $C \gg 1$), and $E_N^{\text{out}}[0] \approx \ln(1+\kappa/\kappa')$ when $\kappa/\kappa' \ll 2C$. In the case of a cavity with tunable external damping rate, the optimal κ satisfies $\kappa = \kappa'\left(\sqrt{2C'}-1\right)$. The corresponding entanglement is $E_N^{\text{out}}[0] \approx \frac{1}{2}\ln(C'/2)$, with $C' = 4G^2/\kappa'\gamma$. This result is the same as the optimal intracavity entanglement, as shown in Eq. (11) of [2] (notice that the definition of C in this paper differs by a factor of 4 comparing with [2]). The maximum entanglement for both spectral entanglement and intracavity entanglement are the same.

2) Resolved peaks case. Including the internal loss and assuming $\kappa_i' = \kappa'$, $\tilde{G} \gg \kappa$, γ, κ'

$$E_N^{\text{out}}[0] \approx 4r - \ln\left(\frac{\kappa + e^{4r}\kappa'}{\kappa+\kappa'} + \frac{e^r \sinh r}{\tilde{C}}\right). \tag{S11}$$

When $\kappa/\kappa' \ll e^{4r}\tilde{C}/(e^{2r}+\tilde{C})$, this reduces to $E_N^{\text{out}}[0] \approx \ln(1+\kappa/\kappa')$. The maximum of entanglement in Eq. (S11) is obtained when $\kappa_{\text{opt}} = \kappa'\left(\sqrt{\tilde{C}\left(1+e^{2r}\right)/2}-1\right)$

$$E_{N,\text{opt}}^{\text{out}}[0] = 4r - \ln\left(1 + \sqrt{\frac{2}{\tilde{C}}}\frac{e^{4r}-1}{\sqrt{e^{2r}+1}} + \frac{1-e^{2r}}{\tilde{C}}\right). \tag{S12}$$

However, notice that in order to have resolved peaks, $\tilde{G} \gg \kappa + \kappa'$. This means the optimal condition is normally not satisfied unless $\kappa' \ll \gamma$.

INFLUENCE OF NON-ROTATING WAVE TERMS

In the main text, we only discussed the dynamics with the rotating wave approximation (RWA), considering the good cavity limit $\kappa \ll \omega_{\text{m}}$. Here we will give the full result including the non-RWA terms and the precise condition to neglect them.

First we notice that the counter-rotating terms are time-independent in the rotating frame with respect to the cavity drives. In this frame, the full Hamiltonian is written as $\hat{H} = \omega_{\text{m}}\left(\hat{b}^\dagger\hat{b} + \hat{d}_1^\dagger\hat{d}_1 - \hat{d}_2^\dagger\hat{d}_2\right) + \hat{H}_{\text{int}} + \hat{H}_{\text{CR}}$ with

$$\begin{aligned}\hat{H}_{\text{int}} &= \left(G_1\hat{b}^\dagger\hat{d}_1 + G_2\hat{b}\hat{d}_2\right) + h.c.\\ \hat{H}_{\text{CR}} &= \left(G_1\hat{b}^\dagger\hat{d}_1^\dagger + G_2\hat{b}\hat{d}_2^\dagger\right) + h.c..\end{aligned} \tag{S13}$$

Thus a closed set of equations in the frequency domain can be obtained

$$\begin{aligned}-i(\omega-\omega_{\text{m}})\hat{b}[\omega] &= -\frac{\gamma}{2}\hat{b}[\omega] - i\left(G_1\left(\hat{d}_1[\omega] + \hat{d}_1^\dagger[\omega]\right) + G_2\left(\hat{d}_2^\dagger[\omega] + \hat{d}_2[\omega]\right)\right) - \sqrt{\gamma}\hat{b}_{in}[\omega]\\ -i(\omega-\omega_{\text{m}})\hat{d}_1[\omega] &= -\frac{\kappa_1}{2}\hat{d}_1[\omega] - iG_1\left(\hat{b}[\omega] + \hat{b}^\dagger[\omega]\right) - \sqrt{\kappa_1}\hat{d}_{in,1}[\omega]\\ -i(\omega-\omega_{\text{m}})\hat{d}_2^\dagger[\omega] &= -\frac{\kappa_2}{2}\hat{d}_2^\dagger[\omega] + iG_2\left(\hat{b}[\omega] + \hat{b}^\dagger[\omega]\right) - \sqrt{\kappa_2}\hat{d}_{in,2}^\dagger[\omega]\end{aligned} \tag{S14}$$

These equations can be solved analytically. Fig. 5 shows the comparison of the results $E_N^{\text{out}}[\omega=0,\sigma=0]$ with/without RWA. The lower curve corresponds to the case where $\tilde{G} > \kappa$ and the normal modes are resolved: counter-rotating

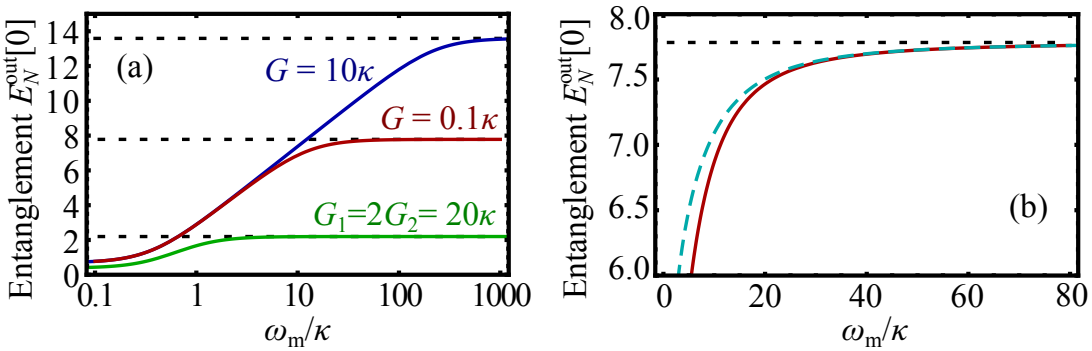

FIG. 5. Validity of the rotating-wave approximation. (a) the solid lines show the output entanglement $E_N^{\rm out}[\omega = 0]$ *vs.* $\omega_{\rm m}/\kappa$ including the counter-rotating terms. From top to bottom, the 3 curves show the case of strong equal-coupling ($G_1 = G_2 = 10\kappa$), weak equal-coupling ($G_1 = G_2 = 0.1\kappa$), resolved peak ($G_1 = 2G_2 = 10\kappa$). The dashed lines mark the results with the rotating wave approximation. For the upper (blue) and lower (green) curve, $\gamma/\kappa = 1\times10^{-3}$, while for the middle curve $\gamma/\kappa = 3.3\times10^{-5}$. (b) shows the comparison of the analytical expression Eq. (S15) (dashed line) with the numerical result (solid line) in the weak coupling case ($G_1 = G_2 = 0.1\kappa$).

terms suppress the entanglement, but become insignificant once $\omega_{\rm m} > \kappa$. The two upper curves correspond to the case with equal-coupling. In the good cavity limit, the maximum entanglement in the equal-coupling regime is much larger than the resolved-peak regime. Consequently, non-RWA corrections play a larger role, and one can only achieve the RWA result deep into the good cavity limit $\omega_{\rm m} \gg \kappa$.

For both equal-coupling and resolved-peak cases, the leading non-RWA correction to $E_N^{\rm out}[0]$ is

$$\delta E_N^{\rm out}[0] \approx -e^{E_N^{\rm out}[0]}\frac{\kappa^2}{16\omega_{\rm m}^2}. \tag{S15}$$

Here $E_N^{\rm out}[0]$ is the entanglement with rotating wave approximation. This approximate expression is shown by the blue dashed line in Fig. 5 (b). Thus the condition to justify the use of RWA is

$$\left|\frac{\omega_{\rm m}}{\kappa}\right| \gg \frac{1}{4}\sqrt{\frac{e^{E_N^{\rm out}}}{E_N^{\rm out}}}, \tag{S16}$$

which is looser in the case of resolved-peaks (due to the smaller $E_N^{\rm out}$).

TIME DELAY TO IMPROVE THE ENTANGLEMENT BANDWIDTH

So far, we have considered the output entanglement with zero bandwidth, i.e., $E_N^{\rm out}[\omega, \sigma = 0, \tau_1]$. However, in practice, the filter function is of finite bandwidth. For simplicity, we consider a square filter function centered at ω with bandwidth σ, i.e.,

$$\hat{D}_i^{\rm out}[\omega, \sigma, \tau_i] = \frac{1}{\sqrt{\sigma}}\int_{\omega-\frac{\sigma}{2}}^{\omega+\frac{\sigma}{2}} d\omega' e^{-i\omega'\tau_i}\hat{d}_i^{\rm out}[\omega']. \tag{S17}$$

Assuming the center frequency is set at $\omega = 0$ (the cavity resonance frequency in the lab frame), the entanglement has a non-trivial dependence on the bandwidth σ and the relative time delay τ_1 (taking $\tau_2 = 0$).

The solid lines of Fig. 3(b) in the main text show the entanglement of the two output cavity modes for zero time delay $E_N^{\rm out}[\omega = 0, \sigma, \tau_1 = 0]$ as a function of bandwidth σ. While the equal-coupling case yields large entanglement at $\sigma = 0$, it is much more sensitive to the increase of the bandwidth. $E_N^{\rm out}[0, \sigma, 0]$ decays on a scale $\sigma \sim C^{-1/4}\gamma$. In contrast, in the resolved normal-mode case, $E_N^{\rm out}[0, \sigma, 0]$ is less sensitive to increasing the mode bandwidth, and is only suppressed significantly when $\sigma \sim \kappa$.

The strong sensitivity to non-zero σ in the case of equal-coupling is related to the change of squeezing phase at different ω. As discussed before, the cavity output state can be characterized by a 2-mode squeezed thermal state (see Eq. (4) in the main text) with a complex squeezing parameter $R_{12}[\omega]$ whose phase is $\theta[\omega] = \arg\left\langle -\hat{D}_1^{\rm out}[\omega]\,\hat{D}_2^{\rm out}[\omega]\right\rangle$

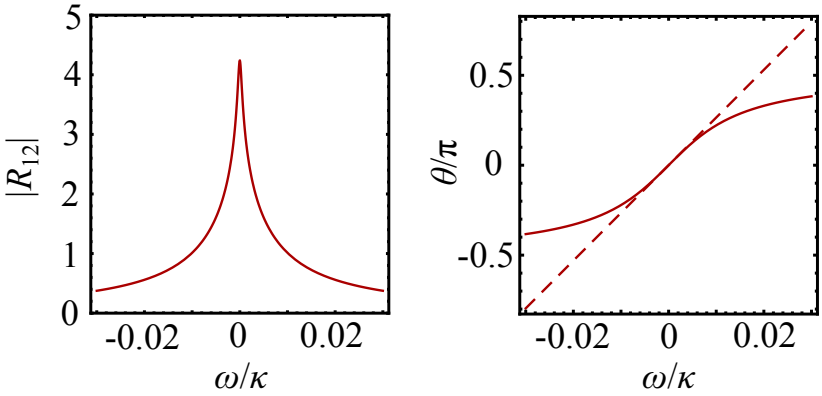

FIG. 6. The dependence of the squeezing parameter R_{12} on frequency. The left panel shows the magnitude change of R_{12}, while the right panel shows the phase change of R_{12}. The dashed line in the right panel is the linear fit given by Eq. (S18). The parameters used are $G/\kappa = 0.1$, $\gamma/\kappa = 3.3 \times 10^{-5}$.

(Eq. (S2)). At $\omega = 0$ and $\sigma = 0$, $R_{12}[0]$ is real (cf. Eq. (7) in the main text), i.e., $\theta = 0$. For $\omega \neq 0$, a frequency-dependent phase arises (see Fig. 6(b)). In the large squeezing limit, i.e., $|R_{12}| \gg 1$ (see Fig. 6(a)), such a phase variation leads to a rapid decrease of entanglement as σ increases. Assuming $\kappa_1 = \kappa_2$ and $G_1 = G_2$ where the magnitude of squeezing is maximized, the peak width of $|R_{12}|$ is comparable to that of $E_N^{\text{out}}[0]$. The corresponding phase variation is approximately linear in the vicinity of $\omega = 0$ (as shown by the dashed linear fit in Fig. 6(b))

$$\delta\theta \approx (\kappa/4G^2)\delta\omega. \tag{S18}$$

This suggests (as per Eq. (S17)), that the optimal entanglement is between a cavity-2 mode emitted at $\tau_2 = 0$ and a cavity-1 mode emitted at $\tau_1 = \kappa/4G^2$. The entanglement with time delay is shown by the red-dashed curve in Fig. 3(b) of the main text. On a heuristic level, our system first generates entangled phonon - cavity 2 photon pairs via the G_2 interaction in Eq. (1) in the main text; next the G_1 interaction swaps the phonon state into a photon in cavity 1. This explains why the optimal entanglement involves a positive delay for the cavity 1 output mode. Finally, we note that for ω away from 0, the squeezing phase θ has a nonlinear frequency dependence, and hence the optimal filter function for larger σ will not correspond to a simple delay as in Eq. (S18).

PHONON OUTPUT THROUGH AN AUXILIARY CAVITY

In optomechanical crystals, a phonon waveguide can be used to access the output of the mechanical system. For a general optomechanical systems where a phonon waveguide is absent, we find it is still possible to access the phonon output by having its damping dominated by optical damping of a third auxiliary cavity. This auxiliary cavity will have a large damping rate, and will be coupled to the mechanics via a linearized optomechanical coupling (the cavity is strongly driven by a red-detuned laser):

$$\hat{H}_{\text{a}} = G_{\text{a}} \left(\hat{b}\hat{d}_{\text{a}}^{\dagger} + \hat{b}^{\dagger}\hat{d}_{\text{a}} \right), \tag{S19}$$

where $\hat{d}_{\text{a}}$ is the annihilation operator of the auxiliary cavity and G_{a} is the corresponding coupling. The auxiliary cavity, due to the large damping rate κ_{a}, can be described by the following steady-state relation:

$$\hat{d}_{\text{a}} = -i\frac{2G_{\text{a}}}{\kappa_{\text{a}}}\hat{b} - \frac{2}{\sqrt{\kappa_{\text{a}}}}\hat{d}_{\text{a}}^{\text{in}}. \tag{S20}$$

Plugging this into the equation of motion for the mechanical resonator one obtains

$$\frac{d}{dt}\hat{b} = -\frac{2G_{\text{a}}^2}{\kappa_{\text{a}}}\hat{b} - i\left(G_1\hat{d}_1 + G_2\hat{d}_2^{\dagger} \right) + \frac{2iG_{\text{a}}}{\sqrt{\kappa_{\text{a}}}}\hat{d}_{\text{a}}^{\text{in}}, \tag{S21}$$

where we have neglected other damping channels of the resonator, supposing that $G_{\rm a}^2/\kappa_{\rm a}$ is sufficiently large. Comparing with the Langevin equation without auxiliary cavity $\frac{d}{dt}\hat{b} = -\frac{\gamma}{2}\hat{b} - i\left(G_1\hat{d}_1 + G_2\hat{d}_2^\dagger\right) - \sqrt{\gamma}\hat{d}_{\rm a}^{\rm in}$ we can identify

$$\hat{b}^{\rm in} = -i\hat{d}_{\rm a}^{\rm in}, \quad \text{and} \quad \gamma = 4G_{\rm a}^2/\kappa_{\rm a}. \tag{S22}$$

The input-output relation of the auxiliary cavity is $\hat{d}_{\rm a}^{\rm out} = \hat{d}_{\rm a}^{\rm in} + \sqrt{\kappa_{\rm a}}\hat{d}_{\rm a}$ which, together with Eqs. (S20) and (S22), gives $\hat{d}_{\rm a}^{\rm out} = -i\sqrt{\gamma}\hat{b} - i\hat{b}^{\rm in}$, thus

$$\hat{d}_{\rm a}^{\rm out} = -i\hat{b}^{\rm out}. \tag{S23}$$

This shows that a strongly damped auxiliary cavity can serve as output of the mechanical mode.

3-MODE ENTANGLEMENT MEASURE BASED ON RÉNYI-2 ENTROPY

The tripartite entanglement can be measured by the residual Gaussian Rényi-2 (GR2) entanglement [3]. The Rényi-2 entropy is given by $S_2(\rho) = -\ln \mathrm{Tr}\left(\rho^2\right)$ and allows to define an entanglement measure $\varepsilon_2(\rho_{A:B})$ for bipartite states ρ_{AB}. For pure states one simply has $\varepsilon_2(\rho_{A:B}) = S_2(\rho_A)$, with ρ_A the reduced density matrix of subsystem A. The tripartite entanglement is then characterized through the residual entanglement $\varepsilon_2(\rho_{i:j:k})$, given by:

$$\varepsilon_2(\rho_{i:j:k}) = \varepsilon_2(\rho_{i:jk}) - \varepsilon_2(\rho_{i:k}) - \varepsilon_2(\rho_{i:j}) \geq 0, \tag{S24}$$

where $i \neq j \neq k = 1,2,3$ represents the 3 different modes (the 3rd mode denotes the mechanics in our case). In Eq. (S24), $\varepsilon_2(\rho_{i:jk})$ is the bipartite entanglement partitioning the global system into $A = i$ and $B = jk$, while $\varepsilon_2(\rho_{i:j})$ and $\varepsilon_2(\rho_{i:k})$ consider the reduced density matrices of subsystems ij and ik, respectively. In general, three different values of $\varepsilon_2(\rho_{i:j:k})$ are obtained, depending on the choice of the "focus mode" i. There are special cases when $\varepsilon_2(\rho_{i:j:k})$ is invariant under mode permutation [3]; as we explain below, that is not the case for our system.

For pure tripartite Gaussian states, $\varepsilon_2(\rho_{i:j:k})$ can be evaluated analytically [3]. The first term of Eq. (S24) is:

$$\varepsilon_2(\rho_{i:jk}) = S_2(\rho_i) = \ln a_i, \tag{S25}$$

where a_i is related to the covariance matrix $\mathbf{V}_i$ of subsystem i:

$$a_i = \sqrt{\det \mathbf{V}_i}. \tag{S26}$$

Using the covariance matrix for our system, calculated from the Langevin equation, it is possible to obtain explicit formulas for $\varepsilon_2(\rho_{1:23})$, $\varepsilon_2(\rho_{2:13})$, $\varepsilon_2(\rho_{3:12})$ in terms of the cooperativities $C_{1,2}$. Although we omit them here, it is worth mentioning that these three quantities are all non-zero, showing that none of the three systems is separable.

The last two terms in Eq. (S24) are given by:

$$\varepsilon_2(\rho_{j:k}) = \frac{1}{2}\ln g_i \quad (i \neq j \neq k).$$

where

$$g_i = \begin{cases} 1, & a_k \geq \sqrt{a_i^2 + a_j^2 - 1}, \\ \frac{\beta}{8a_k^2}, & \alpha_k < a_k < \sqrt{a_i^2 + a_j^2 - 1}, \\ \left(\frac{a_i^2 - a_j^2}{a_k^2 - 1}\right)^2 & a_k \leq \alpha_k, \end{cases} \tag{S27}$$

with

$$\alpha_k = \sqrt{\frac{2\left(a_i^2 + a_j^2\right) + \left(a_i^2 - a_j^2\right)^2 + \left|a_i^2 - a_j^2\right|\sqrt{\left(a_i^2 - a_j^2\right)^2 + 8\left(a_i^2 + a_j^2\right)}}{2\left(a_i^2 + a_j^2\right)}},$$

$$\beta = 2a_1^2 + 2a_2^2 + 2a_3^2 + 2a_1^2a_3^2 + 2a_2^2a_3^2 + 2a_1^2a_2^2 - a_1^4 - a_2^4 - a_3^4 - \sqrt{\delta} - 1,$$

$$\delta = \left((a_1 - a_2 - a_3)^2 - 1\right)\left((a_1 + a_2 - a_3)^2 - 1\right)\left((a_1 - a_2 + a_3)^2 - 1\right)\left((a_1 + a_2 + a_3)^2 - 1\right).$$

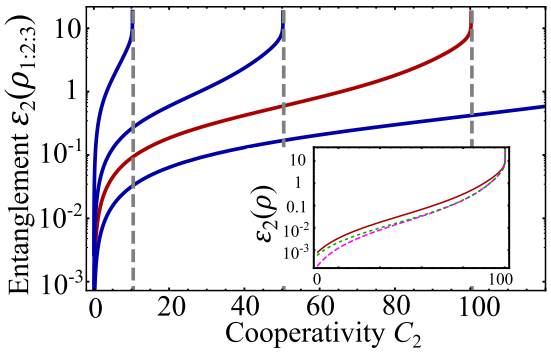

FIG. 7. 3-mode entanglement, evaluated by the residual GR2 entanglement with cavity-1 as the focus mode $\epsilon_2(\rho_{1:2:3})$, versus the cooperativity of cavity 2. Here C_1 is fixed to 10, 50, 100, 200 (from top to bottom). The gray dashed lines indicate the onset of system instability. The 3-mode entanglement diverges at $\gamma_{\rm tot}=0$ or $C_2=C_1+1$. The $C_1=100$ (red) curve is re-plotted in the inset, together with the two residual GR2 entanglement where the focus mode is cavity-2 ($\epsilon_2(\rho_{2:1:3})$) or mechanics ($\epsilon_2(\rho_{3:2:1})$).

Since $\varepsilon_2(\rho_{j:k})$ is the GR2 2-mode entanglement measure in the subspace where the mode i is eliminated, it serves as an alternative way to quantify the 2-mode entanglement in our system, other than the logarithmic negativity used in the main text. We obtain all the two-mode entanglements as follows:

$$\begin{aligned}
\varepsilon_2(\rho_{1:2}) &= \ln\frac{(1+C_2)^2+C_1^2+2C_1+6C_1C_2}{(1+C_2)^2+C_1^2+2C_1-2C_1C_2} \approx \ln\frac{C_2^2+6C_1C_2+C_1^2}{(C_1-C_2)^2}+\mathcal{O}\left(\frac{1}{C_2}\right),\\
\varepsilon_2(\rho_{3:2}) &= \ln\frac{(1+C_1)^2+C_2^2+6C_2+2C_1C_2}{(1-C_2)^2+C_1^2+2C_1+2C_1C_2} \approx \mathcal{O}\left(\frac{1}{C_2}\right),\\
\varepsilon_2(\rho_{1:3}) &= 0,
\end{aligned} \tag{S28}$$

where the last approximation is in the large C limit. These results show that the entanglement between cavity 1 and the mechanics is always zero, although the mechanics is entangled with the composite system of the two cavities ($\varepsilon_2(\rho_{3:12})\neq 0$). In particular, there is entanglement between the mechanics and cavity 2, although it is much smaller than the entanglement between cavity 1 and 2. These results are all in agreement with those based on the logarithmic negativity.

We now turn to the evaluation of the tripartite entanglement $\varepsilon_2(\rho_{i:j:k})$, which is permutationally invariant only when all the $\varepsilon_2(\rho_{i:jk})$ and $\varepsilon_2(\rho_{i:j})$ are non-zero [3]. The fact that $\varepsilon_2(\rho_{1:3})=0$ implies that $\varepsilon_2(\rho_{i:j:k})$ depends on the focus mode, thus we consider all three choices $i=1,2,3$. Using the results for $\varepsilon_2(\rho_{i:jk})$, $\varepsilon_2(\rho_{i:j})$ discussed above, Eq. (S24) gives:

$$\begin{aligned}
\varepsilon_2(\rho_{1:2:3}) &= \ln\left(\frac{C_1^2+(1+C_2)^2+2C_1-2C_1C_2}{(1+C_1-C_2)^2}\right)-2\tanh^{-1}\left(\frac{2C_2}{(1+C_1)^2+6C_1C_2+C_2^2}\right),\\
\varepsilon_2(\rho_{2:1:3}) &= \ln\left(\frac{C_2^2+(1+C_1)^2+6C_2(1+C_1)}{C_2^2+(1+C_1)^2+2C_2(3+C_1)}\right)\\
&\quad+\ln\left(\frac{\left(C_1^2+(1+C_2)^2-2C_1(C_2-1)\right)\left(C_1^2+(1-C_2)^2+2C_1(1+C_2)\right)}{(1+C_1-C_2)^2\left(C_1^2+(1+C_2)^2+2C_1(1+3C_2)\right)}\right),\\
\varepsilon_2(\rho_{3:1:2}) &= \ln\left(\frac{C_2^2+(1+C_1)^2+6C_2-2C_1C_2}{(1+C_1-C_2)^2}\right)-2\tanh^{-1}\left(\frac{4C_2}{(1+C_1-C_2)^2}\right).
\end{aligned} \tag{S29}$$

As announced, the three "residual GR2 entanglements" are unequal. Nevertheless, they are all larger than zero, which confirms the presence of genuine tripartite entanglement. Furthermore, as shown in Fig. 7, the $\varepsilon_2(\rho_{i:j:k})$ all diverge at the instability point $\gamma_{\rm tot}=0$. This divergence is similar to the case of a parametric amplifier and is related to the divergences of $\bar{n}_2$ and $R_{2\rm m}$ as discussed in the main text.

THE TRIPARTITE ENTANGLED OUTPUT STATE

We consider the 3-mode output state $|\Psi\rangle$ (including both cavities and the mechanical resonator) at $\omega = 0$ and $\sigma = 0$. Since $\bar{n}_1 = 0$, see Eq. (7) of the main text, cavity 1 must be in the ground state if we consider the "unsqueezed" state $|\Psi_s\rangle \equiv \tilde{S}_{12}(-R_{12})|\Psi\rangle$. However, $|\Psi_s\rangle$ has residual entanglement between cavity 2 and the mechanical mode. This is clear from the finite value of $\bar{n}_2$, which diverges at the instability condition $\gamma_{\rm tot} = 0$ (the finite population $\bar{n}_2$ is a consequence of tracing out the mechanical mode). One can compute explicitly the correlations of the state $|\Psi_s\rangle$ and identify it as a squeezed vacuum of cavity 2 and the mechanical mode, with squeezing parameter $R_{2\rm m} = \sinh^{-1}\bar{n}_2$. Hence it can be concluded that

$$|\Psi\rangle = \hat{S}_{12}(R_{12})\,\hat{S}_{2\rm m}(R_{2\rm m})\,|000\rangle\,, \tag{S30}$$

with

$$\hat{S}_{2\rm m}(R_{2\rm m}) \equiv \exp\left[iR_{2\rm m}\hat{D}_{\rm m}^{\rm out}[0]\,\hat{D}_2^{\rm out}[0] - h.c.\right]. \tag{S31}$$

Another interesting observation is that, although the tripartite steady state Eq. (S30) is generated by interactions between intracavity modes and the input-output relations, the output state described by Eq. (S30) could also be achieved by a unitary evolution generated by the following interaction between the output modes:

$$\tilde{H} = R_{12}\sin R_{2\rm m}\hat{D}_{\rm m}^{\rm out}[0]\,\hat{D}_2^{\rm out}[0] - R_{2\rm m}\left(\hat{D}_{\rm m}^{\rm out}[0]\right)^{\dagger}\hat{D}_1^{\rm out}[0] + iR_{12}\cos R_{2\rm m}\hat{D}_1^{\rm out}[0]\,\hat{D}_2^{\rm out}[0] + h.c. \tag{S32}$$

This result can be obtained by Wei-Norman decomposition of $\exp\left(-i\tilde{H}\right)$ in terms of the closed algebra $\left\{\left(\hat{D}_{\rm m}^{\rm out}[0]\right)^{\dagger}\hat{D}_1^{\rm out}[0] + h.c., \hat{D}_{\rm m}^{\rm out}[0]\,\hat{D}_1^{\rm out}[0] + h.c., \hat{D}_1^{\rm out}[0]\,\hat{D}_2^{\rm out}[0] - h.c.\right\}$.

Using this effective Hamiltonian, we can derive the expansion of the output state into the Fock state basis:

$$|\Psi\rangle = \exp\left(-i\tilde{H}\right)|000\rangle \tag{S33}$$

$$= \frac{1}{\sqrt{1+\langle N_2\rangle}}\sum_{pq} C_{p+q}^{p}\left(\frac{\langle N_{\rm m}\rangle}{1+\langle N_2\rangle}\right)^{\frac{q}{2}}\left(\frac{\langle N_1\rangle}{1+\langle N_2\rangle}\right)^{\frac{p}{2}}|p, p+q, q\rangle\,, \tag{S34}$$

where

$$\begin{aligned}\left\langle\hat{N}_1\right\rangle &= \frac{4C_1C_2}{(1+C_1-C_2)^2},\\ \left\langle\hat{N}_2\right\rangle &= \frac{4C_2(C_1+1)}{(1+C_1-C_2)^2},\\ \left\langle\hat{N}_m\right\rangle &= \frac{4C_2}{(1+C_1-C_2)^2},\end{aligned} \tag{S35}$$

with p, q integers and $\hat{N}_i \equiv \left(\hat{D}_i^{\rm out}[0]\right)^{\dagger}\hat{D}_i^{\rm out}[0]$ $(i = 1, 2, {\rm m})$. The genuine tripartite entanglement is evident from the perfect correlations between photon and phonon numbers in the output state of Eq. (S34).

[1] L. Tian, Phys. Rev. Lett. **110**, 233602 (2013).
[2] Y.-D. Wang and A. A. Clerk, Phys. Rev. Lett. **110**, 253601 (2013).
[3] G. Adesso, D. Girolami, and A. Serafini, Phys. Rev. Lett. **109**, 190502 (2012).